Lattice dynamics and Mg/Ti order in orthorhombic pseudobrookite-type MgTi$_2$O$_5$

Man He[a], Björn Winkler[a,*], Johannes D. Bauer[a], Lkhamsuren Bayarjargal[a], Javier Ruiz-Fuertes[a,1], Igor Alencar[a,2], Wolfgang Morgenroth[a], Keith Refson[b], Victor Milman[c]

[a]*Institut für Geowissenschaften, Goethe-Universität Frankfurt, Altenhöferallee 1, 60438 Frankfurt am Main, Germany*
[b]*Department of Physics, Royal Holloway, University of London, Egham TW20 0EX, UK*
[c]*Dassault Systèmes BIOVIA, 334 Science Park, Cambridge CB4 0WN, UK*

Abstract

Mg/Ti order/disorder and the lattice dynamics of orthorhombic pseudobrookite-type MgTi$_2$O$_5$ have been studied by experiment and modeling. A mechanochemical activation by high speed ball milling allowed us to synthesize pure MgTi$_2$O$_5$ from MgO and TiO$_2$ anatase at a comparatively low temperature of 1173 K. The Mg/Ti order of MgTi$_2$O$_5$ was characterized by X-ray diffraction and Raman spectroscopy. Density functional theory calculations based on fully ordered MgTi$_2$O$_5$ allow an assignment of all experimentally observed Raman and infrared modes and a re-evaluation of earlier findings. A standard entropy of 134.24 J mol^{-1} K^{-1} and a bulk modulus of 161(1) GPa was predicted for fully ordered MgTi$_2$O$_5$ and is in good agreement with experimental findings based on quasi-adiabatic calorimetry of samples with different Mg/Ti ordering states and earlier high pressure studies, respectively. A linear relation of the $B_{1g}(5)$ Raman blue-shift with the Mg/Ti disorder was observed, which can be used to rapidly quantify the ordering state of MgTi$_2$O$_5$.

Keywords: Mg/Ti order, Mechanochemical activation, Raman spectroscopy, Low-temperature heat capacity, Density functional theory

*Corresponding author
  Email address: b.winkler@kristall.uni-frankfurt.de (Björn Winkler)
  [1]Present address: Departament de Física Aplicada – ICMUV, Universitat de Valéncia, Carrer del Dr. Moliner 50, 46100 Burjassot, Spain
  [2]Present address: Instituto de Física, Universidade Federal do Rio Grande do Sul, Avenida Bento Gonçalves 9500, CEP 91501-970 Porto Alegre-RS, Brazil

1. Introduction

Due to a combination of interesting physical and structural properties, such as a low bulk thermal expansion coefficient [1, 2], a high refractive index [3], the ability to host transition metal ions [4–6], a one-dimensional channel structure [7], and a wide bandgap of 3.4 eV [8], $MgTi_2O_5$ (karrooite) is employed in numerous applications, such as ceramic pigments [3, 9], filter materials [10], UV photocatalysts [11], and anode materials for batteries [7, 12, 13]. According to the $MgO–TiO_2$ equilibrium phase diagram at atmospheric pressure [14–16] $MgTi_2O_5$ is thermodynamically stable over an extended temperature range, limited by melting at $\sim 1953\,K$ and decomposition to $MgTiO_3$ (geikielite) and TiO_2 at temperatures below $\sim 403\,K$ [17]. Due to a large positive entropy at high temperatures [18–21] and the slow kinetics of the Mg/Ti interchange at low temperatures (below 973 K) [15, 18, 19, 22] metastable $MgTi_2O_5$ with an orthorhombic pseudobrookite structure and Mg/Ti disorder can be employed even at lower temperatures [18, 23, 24].

The structure of orthorhombic $MgTi_2O_5$ (figure 1) is commonly described in space group $Cmcm$ (D_{2h}^{17}) [17, 18, 25, 26]. Alternative settings use space groups $Bbmm$ [22, 23] and $Ccmm$ [27]. It consists of edge-sharing and corner-sharing MO_6 octahedra, where M refers to Mg/Ti cations, which are highly distorted and fully occupied by the cations. The $M1$ octahedron (Wyckoff position $4c$ with site symmetry mm) is relatively larger than the $M2$ octahedron (Wyckoff position $8f$ with site symmetry m). As shown in figure 1, the edge-sharing $M2$ octahedra form double chains running along the [010] direction, which are linked through the oxygen bridges O1 and the $M1$ octahedra. Figure 1 shows that the double chains extend in the [100] direction and the bridge oxygens O1 link the octahedra forming corners. The corner-sharing of the $M1$ and $M2$ octahedra is depicted in figure 1. In an ideal fully ordered structure of $MgTi_2O_5$, the larger $M1$ sites are exclusively occupied by the Mg^{2+} ions (mean radius $r_{Mg} = 0.72\,Å$) [28] while the Ti^{4+} ions ($r_{Ti} = 0.605\,Å$) [28] would occupy the $M2$ sites. In reality, part of Mg^{2+} in the $M1$ sites is exchanged by Ti^{4+}, producing Mg/Ti disorder and giving rise to a lattice expansion. The Mg/Ti disorder parameter X, which is defined as the atomic concentration of Ti in $M1$ sites, can be linearly correlated with the ambient-temperature lattice parameter b (corresponds to the lattice parameter a in space group $Bbmm$) according to the equation: $X = 8.6909b – 84.334$ [21]. The Mg/Ti order of $MgTi_2O_5$ is dependent on the thermal history [21]. Usually, quenching from high temperatures leads to an increase of the cation disorder, while annealing at low temperatures or high pressures results in a more ordered structure [21, 22, 29]. Due to the kinetic hindrance, the Mg/Ti disorder attained at high temperatures can be partly or fully retained at ambient conditions [20].

Both solid state syntheses and wet chemical processes have been employed to synthesize $MgTi_2O_5$ [17]. Solid state methods are often preferred over the wet methods because they allow to control the cation

disorder by annealing, quenching and high pressure techniques [21, 30]. In the conventional solid state synthesis of $MgTi_2O_5$, high temperatures above $1673\,K$ are employed [31]. Usually several cycles are required to achieve homogenization and purification, causing a high energy consumption relative to wet methods. Recently a solid formation mechanism of $MgTi_2O_5$ has been proposed, which leads to a reduction of the synthesis temperature to $1273\,K$ [10, 32]. However, it requires adding $0.5\,wt.\%$ of LiF as a mineralizer to the starting materials. LiF acts as a flux [33] and may cause the formation of impurity phases like MgF_2 [15] and $Li_2MgTi_2O_5$ [7]. Here we will show that high energy ball milling, which is increasingly used in the manufacturing of advanced materials [34, 35], can be employed to significantly and reliably decrease the synthesis temperature of single phase $MgTi_2O_5$ without adding any flux.
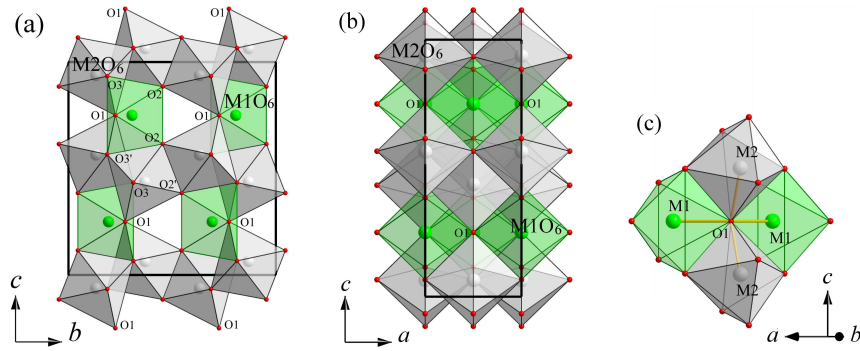

Figure 1: Polyhedral structure of orthorhombic pseudobrookite-type $MgTi_2O_5$ with MO_6 octahedra ($M = Mg/Ti$) in $Cmcm$ space group setting. The red, green and gray spheres denote oxygen atoms, $M1$ sites and $M2$ sites, respectively. The black rectangles show the unit cell dimensions. (a) and (b) present views along [100] and [010], respectively. (c) gives the corner-sharing of 2 $M1$ octahedra and 2 $M2$ octahedra via the bridging oxygen O1.

According to group theory, the orthorhombic pseudobrookite-type $MgTi_2O_5$ has 24 Raman active modes ($8A_g + 5B_{1g} + 3B_{2g} + 8B_{3g}$), 21 infrared modes, of which 18 are optical ($7B_{1u} + 7B_{2u} + 4B_{3u}$) and 3 are acoustic ($B_{1u} + B_{2u} + B_{3u}$), as well as 3 silent modes ($3A_u$). There have been several Raman and infrared spectroscopy studies on $MgTi_2O_5$. Raman spectra have been recorded up to around $1500\,cm^{-1}$ [8, 36]. Liermann et al. [36] have investigated the Mg/Ti order by Raman spectroscopy of oriented $MgTi_2O_5$ single crystals. However, they did not provide an assignment of modes. The published IR spectra suffer from a poor signal-to-noise ratio and only three infrared peaks in the range 400–$1000\,cm^{-1}$ have been identified [8, 37, 38]. In this study, Raman spectra have been obtained for samples at several ordering states and lattice dynamical calculations have been carried out using a model of fully ordered $MgTi_2O_5$ based on density functional perturbation theory (DFPT), which allows an unambiguous assignment of all observed bands.

That the bulk modulus of $MgTi_2O_5$ may depend on the Mg/Ti ordering state has been shown in a

high pressure study of $MgTi_2O_5$, where values for B = 167(1) GPa and B = 158(1) GPa were obtained for fully ordered and disordered single crystals, respectively, but where the pressure range was rather limited, with a maximum pressure of 8 GPa [30]. Up to now the elastic stiffness coefficients of $MgTi_2O_5$ have not been obtained, and in the present study DFT calculations have been employed to probe the elasticity of fully ordered $MgTi_2O_5$, using the experimentally determined bulk modulus of Hazen and Yang [30] as a benchmark.

For a deeper understanding of the stability, the thermodynamic properties (enthalpy, entropy and Gibbs free energy) need to be known. The molar Gibbs free energy of $MgTi_2O_5$ consists of a configurational contribution as well as a lattice vibrational contribution [19]. The configurational contribution, $-TS_{config}$, depends on the Mg/Ti disorder [18–21]. In earlier studies several thermodynamic models have been constructed. The model parameters, which depend on the temperature and pressure, are fitted by using the experimental Mg/Ti disorder data at high (p, T) conditions as well as the measured high-temperature relative enthalpies [19–21]. The temperature dependence of the heat capacity of a $MgTi_2O_5$ powder sample (197 g, purity ≈99.5%) was measured between 50 K and 298 K from which a vibrational entropy of $127.2(8) \, J \, mol^{-1} \, K^{-1}$ [39] at ambient temperature was obtained. Unfortunately, no detailed information regarding the ordering state of the sample was included in the study by Todd [39]. Here, we have measured the low-temperature heat capacities of $MgTi_2O_5$ with different Mg/Ti disorder parameters in a more extended temperature range of 2–300 K and have calculated the vibrational entropies and enthalpies of $MgTi_2O_5$.

2. Experimental and computational approaches

2.1. Sample preparation

Powder samples of MgO and TiO_2 anatase (purity 99%, Merck, Germany) were used. The MgO was pre-calcined at 1073 K for 2 h. A mixture of the oxides with a stoichiometric molar ratio of 1:2 was first ball milled at 300 rpm for 3 h using a planetary ball mill (Fritsch P7, Germany). Tungsten carbide milling balls (diameter of 10 mm) and bowls (volume 80 mL) were used and the mass ratio of balls to powder was 20:1. Then the mixture was pressed into cylinders (diameter of 5 mm and height of 10 mm), followed by heat-treatments at 1073–1473 K in air for 4–96 h. Finally, the samples were cooled down by turning off the furnace and were ground into fine powders for further characterizations. As a reference, the stoichiometric mixture without ball milling was ground, pressed, heat-treated at 1273–1473 K in air and then cooled within the furnace.

2.2. X-ray powder diffraction

X-ray powder diffraction data (XPRD) were collected on a X'Pert Pro X-ray diffractometer (PANalytical) (40 kV, 30 mA) with Bragg-Brentano geometry over a 2θ range 10–140° using Cu$K\alpha_1$ radiation (λ = 1.5406 Å) at ambient conditions. In the incident beam path, a curved Ge(110) monochromator, 0.5° divergence slit and 15 mm brass mask were mounted. Silicon powder was added as an internal standard for a long measurement with collecting times of around 17 h, using a step size of 0.002° and the time per step of 200 s.

Rietveld refinements of the XPRD data with pseudo-Voigt profile function were carried out using the GSAS program [40] and the EXPGUI interface [41]. Initial cell and atomic parameters of $MgTi_2O_5$ and TiO_2 rutile were taken from the literature [21, 42]. The background was well fitted by a Chebyshev polynomial with 8 terms. All atom displacement parameters were constrained to be isotropic and composition was assumed to be stoichiometric. Due to the small difference in the scattering power between the Mg^{2+} ion and the Ti^{4+} ion for 8 keV X-rays, the site occupancy was not refined but calculated from the ambient-temperature lattice parameter b using the linear relation mentioned earlier [21].

2.3. Micro-Raman spectroscopy

Raman spectra of powders were collected in quasi-backscattering configuration without polarization analysis at ambient conditions with a micro-Raman spectrometer (Renishaw) using the 532 nm line of an Nd:YAG laser (manufacturer Lightwave). The spectral region ranged from 100 cm^{-1} to 1500 cm^{-1}. In order to avoid sample degradation, the laser output power was kept at 20 mW and the sample was exposed for 10 s. A 1800 groove mm^{-1} grating was used and the Rayleigh line filtered with an edge filter. The spectral resolution was 2 cm^{-1}.

2.4. Quasi-adiabatic micro-calorimetry

Two small pellets with dimensions 2×2×0.5 mm were cut from the sample milled for 3 h and sintered at 1473 K. One pellet was measured without further treatment while the other one was enclosed in Pt foil and annealed at 873 K for 1500 h (62.5 days) in order to increase the Mg/Ti order. Low-temperature heat capacities of the two pellets were measured in the range 300–2 K using a physical properties measurement system (PPMS, Quantum Design). At each temperature, the response to a heat pulse was measured three times. The heat capacities of the empty holder containing Apiezon N grease, with which the sample was thermally coupled to the sample holder, was measured and subtracted from the data for the samples. The enthalpies and entropies of $MgTi_2O_5$ were calculated after fitting the measured heat capacity data by high-order polynomials for different temperature ranges.

2.5. Density functional theory

DFT calculations for a fully ordered $MgTi_2O_5$ model were performed with commercial and academic versions of the CASTEP program using the generalized gradient approximation (GGA) formalized by Perdew-Burke-Ernzerhof (PBE) with a plane wave basis set and norm-conserving pseudopotentials from the CASTEP data base [43, 44]. The maximum cutoff energy of the plane waves was 990 eV. The calculations were carried out using a primitive cell, where a 8×8×4 Monkhorst-Pack grid was employed corresponding 40 k-points in the irreducible part of the Brillouin zone with a k-point separation less than $0.036 \,\text{Å}^{-1}$. Lattice dynamical properties of fully ordered $MgTi_2O_5$ and related thermodynamic properties were obtained using density functional perturbation theory, DFPT [45] in the harmonic approximation. For the sampling of the phonon density of states a 3×2×7 Monkhorst-Pack set was employed, giving a maximum spacing of 0.049 Å^{-1} between points. Raman activities were obtained from a hybrid DFPT/finite displacement approach [46] as implemented in CASTEP [45]. Elastic stiffness coefficients were obtained from stress-strain relations [47]. Full geometry optimisations were carried out until forces were smaller than 0.01 eV/Å and no component of the stress tensor exceeded 0.02 GPa. This resulted in a ground state structure with lattice parameters of $a = 3.7317 \,\text{Å}$, $b = 9.7919 \,\text{Å}$ and $c = 10.1112 \,\text{Å}$, which agree to within 0.5% of the experimental values [21].

3. Results and discussion

3.1. Mg/Ti order

After 3 h of ball milling, no reaction occurred and the average crystalline sizes of the starting materials (TiO_2 anatase and MgO) decreased to around 500 nm, as estimated by applying the Scherrer equation to diffraction data [48, 49]. Pure $MgTi_2O_5$ was obtained after a heat-treatment at 1173 K. Figure 2 shows the Rietveld refinement results (in a selected 2θ range of 10–75°) of XPRD data for the pure $MgTi_2O_5$.

Table 1 summarizes the synthesis conditions and refinement results. The required synthesis temperature could be decreased from 1373 K to 1173 K by 3 h of ball milling. The Mg/Ti disorder parameter X varied from 0.30(1) to 0.37(1) and drastically decreased to 0.14(1) on annealing at 873 K. With increasing disorder, the average $M1$–O1 bond length decreased while the average $M2$–O1 bond length increased, in accordance with data published earlier [21, 22]. In all refinements, the thermal displacement parameter was fixed to be $0.006 \,\text{Å}^2$ for cations and $0.01 \,\text{Å}^2$ for oxygen anions. R_{wp} factors are relatively high and χ^2 are around 1. This is mainly due to the relative low intensity of the Bragg reflections with respect to the background [50, 51]. However, the refinements converged quite satisfactorily, as indicated by figure 2.

The dependence of the Mg/Ti disorder parameter X on the synthesis conditions of $MgTi_2O_5$ is depicted in figure 3 where earlier experimental data [18, 22] and thermodynamic models [19, 20] are also plotted. In

Table 1: Synthesis conditions and Rietveld refinement results of $MgTi_2O_5$ with space group $Cmcm$ and $Z = 4$. Thermal displacement parameters were fixed to reasonable values: $U_{iso}(M1) = U_{iso}(M2) = 0.006\,\text{Å}^2$, $U_{iso}(\text{oxygen}) = 0.01\,\text{Å}^2$. Estimated standard deviation (esd.) in the last decimal digit are indicated with parentheses. [a]Profile R-factor $R_p = \frac{\sum |I_o - I_c|}{\sum I_o}$, where I_o and I_c denote the observed and computed intensities, respectively [40]. [b]Weighted profile R-factor $R_{wp} = \sqrt{\frac{\sum w(I_o - I_c)^2}{\sum wI_o^2}}$, where w is the weight. [c]Goodness of fit $\chi^2 = \frac{R_{wp}^2}{R_{exp}^2}$, with $R_{exp}^2 = \frac{N}{\sum wI_o^2}$ and N, the number of data points. [d]The Mg/Ti disorder parameters X are calculated values: $X = 8.6909b - 84.334$ [21].

|							
Milling time [h]	0	0	3	3	3	3	3
Sintering temperature [K]	1373	1473	1173	1273	1373	1473	1473
Sintering time [h]	4	4	15	4	4	4	4
Annealing temperature [K]	-	-	-	-	-	-	873
Annealing time [h]	-	-	-	-	-	-	1500
Purity [wt. %]	98(1)	99(1)	100	100	100	100	100
a [Å]	3.7439(1)	3.7433(1)	3.7448(1)	3.7437(1)	3.7444(1)	3.7456(1)	3.7386(1)
b [Å]	9.7384(1)	9.7381(1)	9.7422(1)	9.7422(1)	9.7432(1)	9.7463(1)	9.7192(1)
c [Å]	9.9956(1)	10.0012(1)	9.9958(1)	9.9989(1)	9.9960(1)	9.9939(1)	10.0160(1)
V [Å^3]	364.44(1)	364.57(1)	364.67(1)	364.67(1)	364.71(1)	364.84(1)	363.95(1)
$M1$–O1 length [Å]	2.014(1)	2.025(3)	2.023(1)	2.026(1)	2.017(1)	1.975(2)	2.076(2)
$M2$–O1 length [Å]	2.067(1)	2.054(4)	2.065(1)	2.059(1)	2.075(1)	2.109(2)	2.011(2)
O1–$M1$–O1 angle [°]	136.8(1)	135.1(4)	135.4(2)	134.9(1)	135.5(4)	143.1(3)	128.4(2)
R_p [a] [%]	16.7	12.9	15.1	13.6	13.5	15.1	15.9
R_{wp} [b] [%]	26.4	20.8	22.2	21.7	20.5	24.9	25.8
χ^2 [c]	1.10	1.09	0.98	1.04	1.01	1.15	1.15
Disorder parameter X [d]	0.30(1)	0.30(1)	0.33(1)	0.33(1)	0.34(1)	0.37(1)	0.14(1)
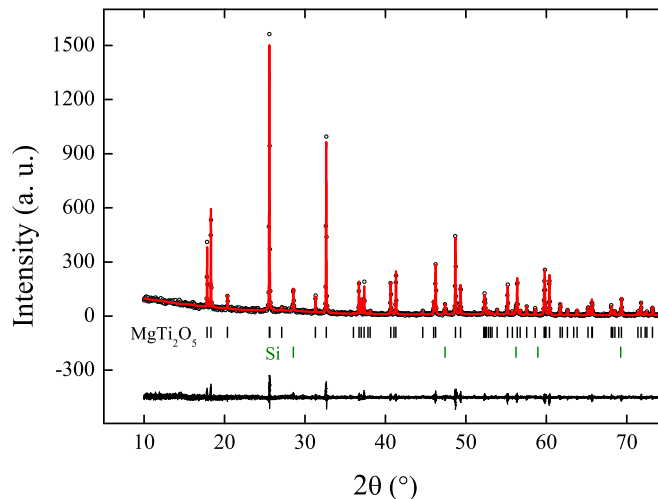
Figure 2: Rietveld refinement results of XPRD data for the pure $MgTi_2O_5$ which was synthesized at 1173 K. 10 wt% silicon powder was added as an internal standard in $MgTi_2O_5$. The bottom black curve represents the difference between the observed data (black circles) and the calculated (continuous red curve) data. The bottom tickmarks indicate the location of Bragg reflections for the crystalline phases.

the temperature range 1273–1473 K, the X values obtained here are lower than the reported experimental data [18, 22] due to the short holding time and the slow cooling rate from the synthesis temperature in this study. The figure shows that ball milling prior to the heat-treatment causes an increase of the Mg/Ti disorder. When annealed at low temperature our data match the T-independent model of Xirouchakis et al. [20] very well.

3.2. Vibrational properties

Raman spectra of the $MgTi_2O_5$ samples with differing ordering states are shown in figure 4. The spectra were normalized to the most intense band in the sample with the least disorder $[X = 0.14(1)]$ to facilitate a comparison. Due to the significant broadening present in all samples, only 12 Raman modes were unambiguously identified. For the samples with a larger X value, only 9 bands could be identified. As the Mg/Ti disorder increases, the mode at $640(2)\,cm^{-1}$ shows the largest blue-shift within the resolution of our Raman spectrometer $(\pm 2\,cm^{-1})$.

Figure 5 shows a comparison of the theoretical Raman spectrum of fully ordered $MgTi_2O_5$ to the measured Raman spectrum of $MgTi_2O_5$ with $X = 0.14(1)$, and gives a plot of the theoretical Raman shifts of $MgTi_2O_5$ against the experimentally determined values. Calculated spectra are normalized to the peak intensity of the first $B_{1g}(1)$ Raman mode. The agreement between the relative peak intensities with respect
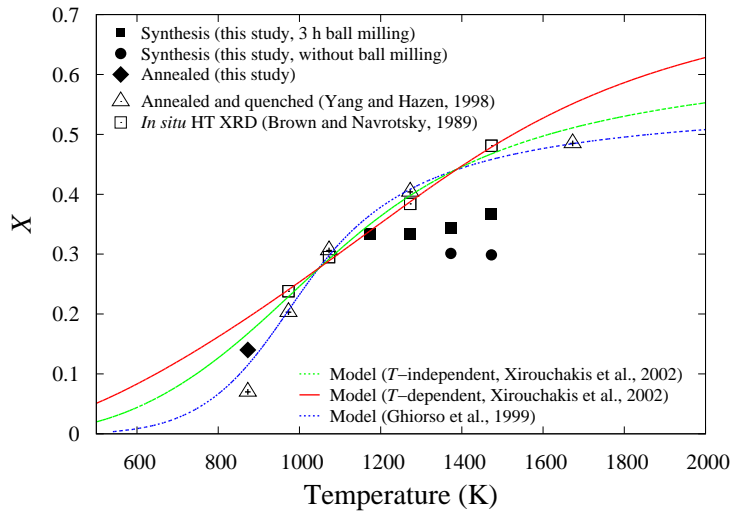
Figure 3: Dependence of the Mg/Ti disorder parameter X on the synthesis conditions of $MgTi_2O_5$. $MgTi_2O_5$ obtained with and without a mechanochemical activation process by ball milling is shown by the filled squares and circles, respectively. The filled diamond denotes $MgTi_2O_5$ annealed at $873\,K$. The open triangles indicate experimental data for $MgTi_2O_5$ single crystals quenched from different annealing temperatures [22], while the open squares represent the results from *in situ* high-temperature X-ray powder diffraction measurements [18]. The T-independent and T-dependent thermodynamic models [19] were constructed by using the former data [18] while the model with blue dashes [20] was based on the latter experimental data [22].

to this Raman mode is outstanding. The agreement for the frequencies is very good except for the mode at $640(2)\,cm^{-1}$ which is a $B_{1g}(5)$ Raman mode according to the calculations. Table 2 shows the frequencies and assignment of our calculated and observed Raman modes, as well as those previously reported in the literature [8, 36]). The assignments were based on the frequencies and intensities. The theoretical Raman spectrum of fully ordered $MgTi_2O_5$ shows Raman shifts between 100–$800\,cm^{-1}$, a much more limited frequency range than previously reported by Liermann et al. [36] who assigned Raman modes up to $1500\,cm^{-1}$. Only one higher frequency mode was observed in our experiments at around $902(2)\,cm^{-1}$ which can be assigned to an overtone due to the combination of the $B_{1g}(3)$ mode at $251(2)\,cm^{-1}$ and $B_{1g}(5)$ mode at $650(2)\,cm^{-1}$. This band is very likely identical to the previously reported Raman bands at $915\,cm^{-1}$ and $913\,cm^{-1}$ [8, 36].

We conclude that the noticeable disagreement between the computed and experimentally observed $B_{1g}(5)$ Raman mode is due to the sensitivity of this mode on the cation disorder, which was not included in the

Table 2: Theoretical and experimental [8, 36] Raman shifts ν (cm^{-1}) and Raman activities γ (Å^4/amu) of MgTi$_2$O$_5$. The DFT calculations are based on fully ordered MgTi$_2$O$_5$ ($X = 0$).

| Theory | | | Experimental results | | | | |
| $X = 0$ | | | $X = 0.14(1)$ | $X = 0.37(1)$ | $X = 0.070$ [36] | $X = 0.485$ [36] | X unknown [8] |
Γ_{Raman}	ν	γ	ν	ν	ν	ν	ν
$B_{1g}(1)$	144	201	155.4(5)	160.3(5)	165.3(3)	168(1)	165
$B_{2g}(1)$	146	7					
$B_{3g}(1)$	193	9					
$A_g(1)$	197	17					
$B_{1g}(2)$	200	28	199.6(5)	204.6(5)	206.8(3)	198(1)	207
$B_{2g}(2)$	203	10					
$B_{1g}(3)$	245	243	250.1(5)	251.4(5)		260.7(5)	259
$A_g(2)$	256	153	263(1)	264.7(5)	270.34(3)	274(2)	
$B_{3g}(2)$	278	11					
$B_{3g}(3)$	284	8					
$A_g(3)$	321	135	324.4(5)		329.1(1)	323.8(8)	
$A_g(4)$	364	29	364.5(5)	359(1)	369.9(1)	356(1)	
$B_{3g}(4)$	384	66	390.0(5)				
$A_g(5)$	415	85	417.1(5)		421.9(1)	448(2)	
$B_{3g}(5)$	448	4					
$B_{1g}(4)$	473	249	477.4(5)	483.8(5)	499(13)		491
$A_g(6)$	477	61					
$B_{3g}(6)$	488	27					
$A_g(7)$	519	11			522(1)		
$B_{2g}(3)$	579	14				593(3)	
$B_{1g}(5)$	604	790	640.1(5)	649.4(5)	632(1)	653(3)	654
$B_{3g}(7)$	633	7					
$B_{3g}(8)$	766	8					
$A_g(8)$	775	1137	784.4(5)	782.5(5)	789.92(1)	779.2(1)	798
Overtone	849		901(1)	902(1)	913.0(2)	908.7(4)	915
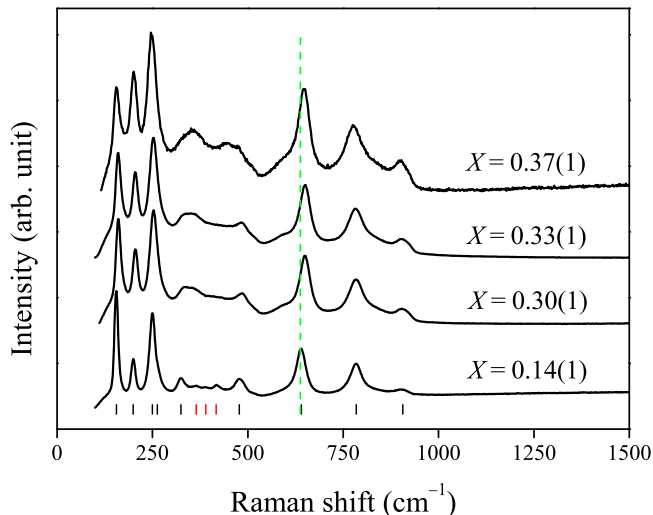
Figure 4: Raman spectra of disordered $MgTi_2O_5$. The dashed line is a guide to the eye highlighting the Raman shift. The tickmarks show the observed Raman band positions where the three in red color are only valid for $X = 0.14(1)$.
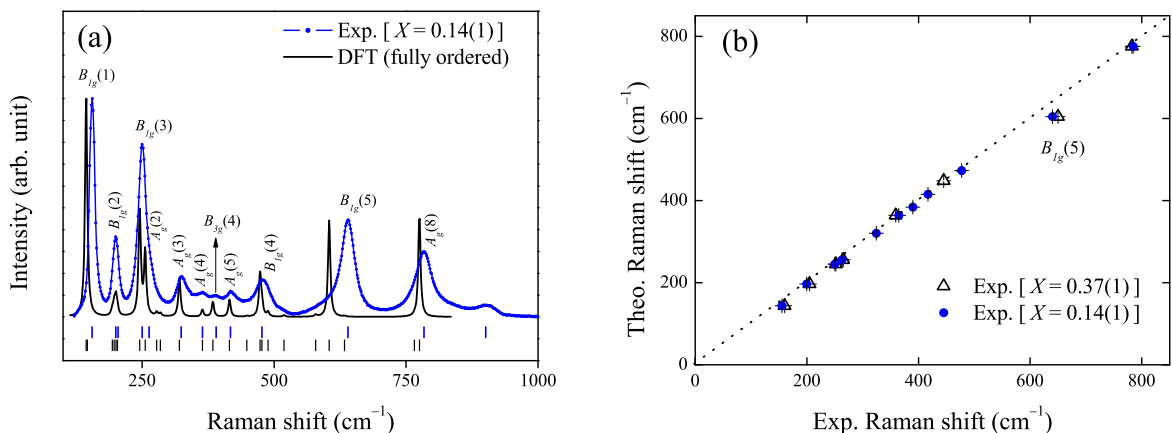

Figure 5: (a) The theoretical Raman spectrum with band assignment of fully ordered $MgTi_2O_5$, compared to the measured Raman spectrum of $MgTi_2O_5$ with $X = 0.14(1)$. Calculated spectra are normalized to the intensity of the first $B_{1g}(1)$ Raman mode. (b) The theoretical Raman shifts of $MgTi_2O_5$ against the experimentally determined values.

simulation. An analysis of our data and data published earlier [36] shows that the frequency, ω, of the $B_{1g}(5)$ mode of $MgTi_2O_5$ linearly depends on the Mg/Ti disorder parameter X: $\omega = 629(1)\,\mathrm{cm}^{-1} + 60(5)\,X\,\mathrm{cm}^{-1}$ (R-square $= 0.91$), as indicated in figure 6. This provides a convenient way for the rapid quantification of the Mg/Ti ordering state of $MgTi_2O_5$.

In order to understand the high sensitivity of the $B_{1g}(5)$ Raman mode on X, we have calculated its eigenvector. A sketch is shown in figure 7. This mode consists of an anti-phase stretching of two $M2$–O1 bonds and a concomitant bending of two $M1$–O1 bonds where the two $M2$ octahedra and the two $M1$
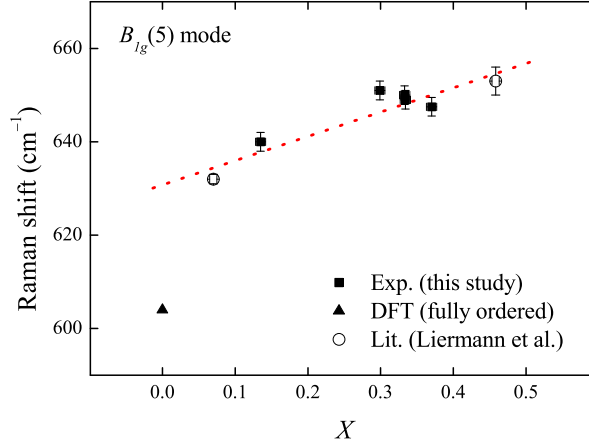
11

Figure 6: Frequencies of the observed $B_{1g}(5)$ Raman mode against the parameter X. The filled squares are experimental data from this study, while the open circles presents data from the literature [36]. The dashed line is the linear fit of the two data sets which were assumed to carry equal weight. As a comparison, the calculated datum from the DFT calculations is plotted in the filled triangle.

octahedra share the same corner (figure 1). This mode has an unusual displacement pattern in that it consists of an oxygen displacement nearly parallel to [001], while all other atoms essentially remain stationary. Given the nature of this mode, its frequency is expected to be very sensitive to the changes of the $M1$–O1 and $M2$–O1 bonds. The Rietveld refinement results (table 1) show that the lattice parameter c decreases with increasing disorder, while the $M1$–O1 bond length decreases and the $M2$-O1 bond length increases. While the contribution of each of the three effects cannot be readily quantified, they add up in such a way that the $B_{1g}(5)$ mode blue-shifts significantly with increasing disorder.
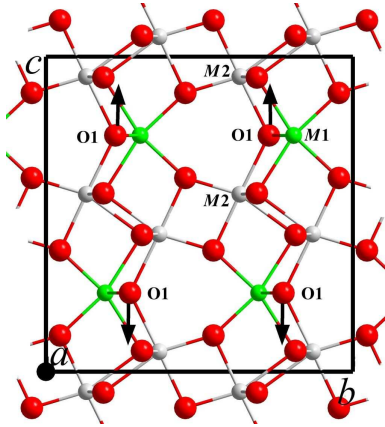

Figure 7: Oxygen O1 motions corresponding to the $B_{1g}(5)$ Raman mode of fully ordered $MgTi_2O_5$ in (100) plane. The red, green and gray spheres denote oxygen atoms, $M1$ sites and $M2$ sites, respectively. Bonds between the Mg/Ti cations and the oxygen anions are shown. The eigenvector is depicted by black arrows.

12

The computed infrared absorption of fully ordered $MgTi_2O_5$ is depicted in figure 8. Wavenumbers and representations of the 18 infrared-active modes are tabulated in table 3, excluding the three acoustic modes with B_{1u}, B_{2u} and B_{3u} symmetry.
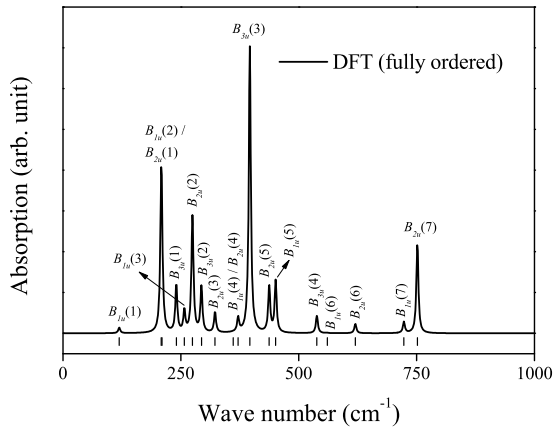

Figure 8: The computed infrared absorption of fully ordered $MgTi_2O_5$.

We tentatively assigned the experimentally determined infrared modes of disordered $MgTi_2O_5$ at around $426\,cm^{-1}$, $505\,cm^{-1}$ and $648\,cm^{-1}$ [37, 38] to $B_{3u}(3)$, $B_{3u}(4)$ and $B_{2u}(6)$ modes, respectively. The deviation between our theoretical infrared absorption bands and the reported experimental values is 5–9%, which is still a reasonable agreement, as the experimentally determined spectra are of low quality and the ordering state of the samples is unknown.

3.3. Elasticity

Table 4 lists the 9 independent elastic stiffness coefficients c_{ij} of fully ordered $MgTi_2O_5$ derived from DFT calculations. The compression coefficients (c_{11}, c_{22} and c_{33}) as well as the shear coefficients (c_{44}, c_{55} and c_{66}) show some anisotropy. The compressibility is smallest along the [100] direction and largest along the [001] direction, which is, as expected, similar to the correlation observed in thermal expansion measurements [25]. Our elastic parameter calculations yielded a bulk modulus of $161(1)\,GPa$ for fully ordered $MgTi_2O_5$, which is close to the reported value of $167(1)\,GPa$ [30]. Figure 9 is the representation surface of the longitudinal stiffness of the fully ordered $MgTi_2O_5$ structure, showing only a moderate anisotropy.

3.4. Low-temperature thermodynamic properties

Figure 10 depicts the theoretical and experimental low-temperature heat capacities C_p of $MgTi_2O_5$. The theoretical values were obtained from DFT calculations of fully ordered $MgTi_2O_5$. They are in reason-

Table 3: Infrared vibrational modes ν (cm^{-1}) and IR activity γ (Debye/Å^2/amu) of fully ordered MgTi$_2$O$_5$ from DFT calculation and experimental IR frequencies taken from the literature [37, 38]. The three acoustic modes are not included.

Theory			Experimental results	
$X=0$			$X=0.11$ [37]	$X=0.34$ [38]
Γ_{IR}	ν	γ	ν	ν
$B_{1u}(1)$	119	3		
$B_{1u}(2)$	208	94		
$B_{2u}(1)$	210	4		
$B_{3u}(1)$	240	27		
$B_{1u}(3)$	257	12		
$B_{2u}(2)$	275	68		
$B_{3u}(2)$	294	26		
$B_{2u}(3)$	322	12		
$B_{1u}(4)$	361	0.1		
$B_{2u}(4)$	371	8		
$B_{3u}(3)$	396	166		425.99
$B_{2u}(5)$	437	27		
$B_{1u}(5)$	451	30		
$B_{3u}(4)$	538	10	509.8	505.30
$B_{1u}(6)$	561	0.2		
$B_{2u}(6)$	620	6	641.2	648.03
$B_{1u}(7)$	723	6		
$B_{2u}(7)$	752	52		

able agreement with our measured C_p values and the experimental C_p determined by Todd [39]. Further thermodynamic properties are tabulated in table 5 and compared with data from the literature [39].

Assuming an equilibrium and random Mg/Ti distribution in each octahedral site of MgTi$_2$O$_5$ at a given temperature, the configurational entropy S_{config} can be derived from the disorder parameter X by equation 1 [18, 19, 53], which is plotted in figure 11. The standard configurational entropies $S_{\mathrm{config}}^{\circ}$ of MgTi$_2$O$_5$ at 298 K are tabulated in table 5. They are 0, 7.6(4) and 13.4(2) J mol^{-1} K^{-1} for fully ordered and the disordered MgTi$_2$O$_5$ with $X = 0.14(1)$ and $X = 0.37(1)$, respectively.

Table 4: Elastic stiffness coefficients c_{ij} of the fully ordered $MgTi_2O_5$ from theory in GPa. The resulting bulk modulus K is predicted to be 161(1) GPa, in good agreement with an experimentally determined value of 167(1) GPa [30].

i	j	c_{ij}
1	1	300(1)
2	2	269(1)
3	3	244(1)
4	4	76(1)
5	5	85(1)
6	6	53(1)
1	2	145(1)
1	3	105(1)
2	3	87(1)

Table 5: Standard enthalpies and entropies of $MgTi_2O_5$ at 298 K from this study and the literature [20, 39]. Values shown in parentheses are esd. in the last decimal place.

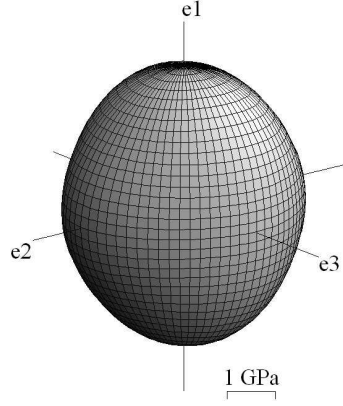|	$X = 0$ (DFT)	$X = 0.14(1)$ (Exp.)	$X = 0.37(1)$ (Exp.)	$X = 0$ (Model) [20]	X unknown (Exp.) [39]
H_{vibra}° [kJ mol^{-1}]	23.43	22.12(3)	22.78(3)	-	-
S_{vibra}° [J mol^{-1} K^{-1}]	134.24	124.8(1)	129.4(1)	-	127.2(8)
S_{config}° [J mol^{-1} K^{-1}]	0	7.6(4)	13.4(2)	-	-
S° [J mol^{-1} K^{-1}]	134.24	132.4(4)	142.8(2)	149.55	-

Figure 9: Representation surface of the longitudinal elastic stiffness of the fully ordered $MgTi_2O_5$. The representation surface was plotted using the WinTensor^{TM} software [52].
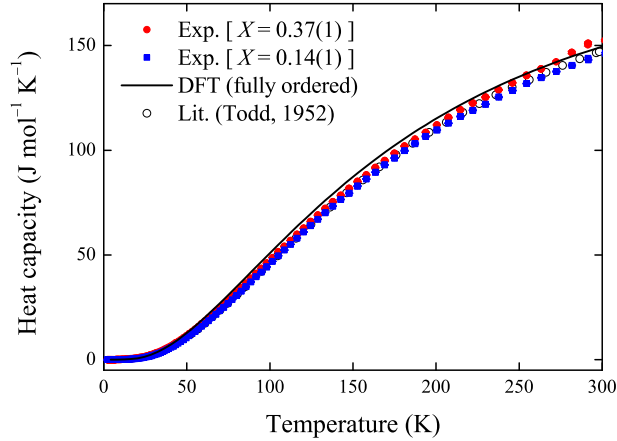

Figure 10: Low-temperature heat capacities C_p of $MgTi_2O_5$. The continuous black curve shows the theoretical data of fully ordered $MgTi_2O_5$ from DFT calculations. The filled blue squares and the filled red circles show the measured data of $MgTi_2O_5$ from this study up to $300\,\mathrm{K}$ with $X = 0.14(1)$ and $X = 0.37(1)$, respectively. The open circles are the reported experimental data of $MgTi_2O_5$ with an unknown X in the temperature range 50–$300\,\mathrm{K}$ [39].

$$S_{\mathrm{config}} = -R[X \ln X + (1 - X)\ln(1 - X) + X \ln(X/2) + (2 - X)\ln(1 - X/2)] \tag{1}$$

with the gas constant $R = 8.314\,\mathrm{J\,mol^{-1}\,K^{-1}}$.

For these two ordering states, the difference in the vibrational entropy is $4.6(2)\,\mathrm{J\,mol^{-1}\,K^{-1}}$ at $298\,\mathrm{K}$, which has the same magnitude as the excess configurational entropy of $5.9(6)\,\mathrm{J\,mol^{-1}\,K^{-1}}$. The increase of the disorder parameter X from $0.14(1)$ to $0.37(1)$ leads to a change in the temperature dependence of the heat capacity and entropy. Figure 12 shows the experimentally determined differences in the vibrational enthalpies and entropies between two $MgTi_2O_5$ samples with differing ordering states $X = 0.14(1)$ and X
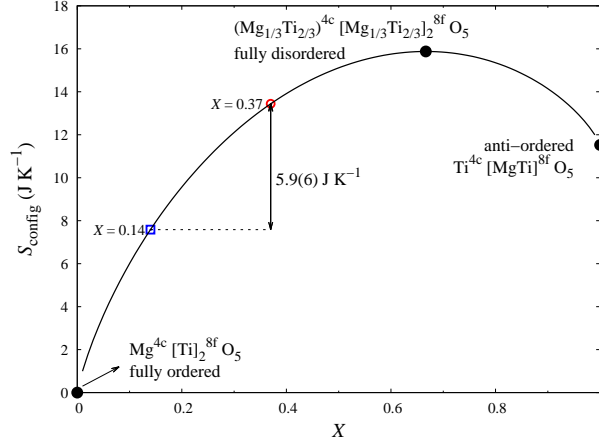
Figure 11: Dependence of the configurational entropy of $MgTi_2O_5$ on the disorder parameter X. An excess S_{config} of $5.9(6)\,J\,mol^{-1}\,K^{-1}$ with the increase of the disorder parameter from $X = 0.14(1)$ (the blue square) to $X = 0.37(1)$ (the red circle) is marked. The calculation is based on equation 1.
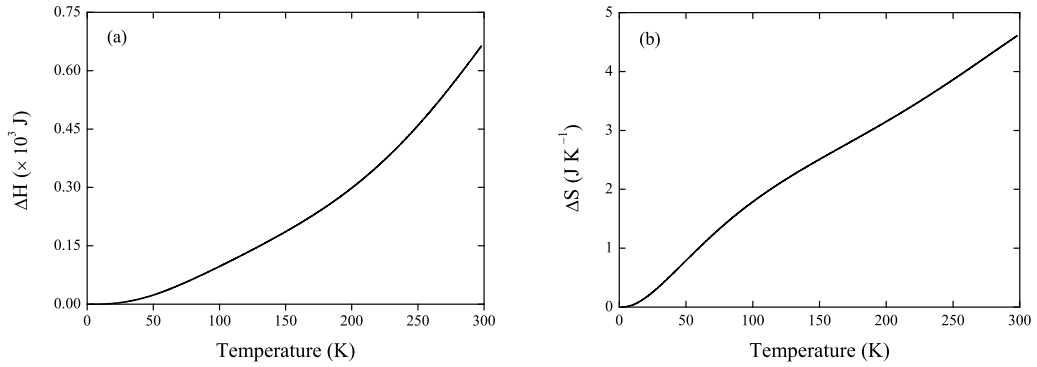
$= 0.37(1)$, respectively.

Figure 12: Low-temperature excess vibrational enthalpy (a) and entropy (b) between the two disordered $MgTi_2O_5$ with $X = 0.37(1)$ and $X = 0.14(1)$.

Table 5 presents the total standard entropies S° of $MgTi_2O_5$ from the experiments and the calculations [20]. The agreement between them is good. However, the corresponding excess vibrational enthalpy of $0.66(5)\,kJ\,mol^{-1}$ is around an order of magnitude smaller than the total excess enthalpy of $5.8(5)\,kJ\,mol^{-1}$ deduced in an earlier thermodynamic modeling study by Xirouchakis et al. [20]. Also, an extrapolation of our experimental data for fully ordered $MgTi_2O_5$ leads to a standard entropy of $126.1\,J\,mol^{-1}K^{-1}$, significantly lower than the "preferred value" of $149.55\,J\,mol^{-1}K^{-1}$ in the earlier study by Xirouchakis et al. [20]. As our data set is more complete, and as there is good agreement between our new data with other spectroscopic and calorimetric data data, we conclude that our findings are likely to be more reliable than those derived

17

from thermodynamic modeling.

4. Conclusion

The solid state synthesis of $MgTi_2O_5$ compound is facilitated by high speed ball milling, which leads to a drastically reduced synthesis temperature of $1173\,K$ compared to $1373\,K$ without ball milling. A pre-milling process results in a more disordered structure. Reliable predictions of vibrational, elastic and thermodynamic properties have been achieved by DFT calculations based on fully ordered $MgTi_2O_5$, all of which are in good agreement with experimental data. A comparison between the experimental and the theoretical Raman and IR spectra of $MgTi_2O_5$ shows that the vibrational properties are sensitive to the Mg/Ti disorder. Particularly, the $B_{1g}(5)$ Raman mode blue-shifts significantly and linearly with increasing Mg/Ti disorder, which allows a rapid quantification of the ordering state of $MgTi_2O_5$. According to the calculation, fully ordered $MgTi_2O_5$ exhibits an elastic anisotropy which makes the [001] direction slightly more compressible than the [100] direction. The standard entropy of fully ordered $MgTi_2O_5$ was predicted to be $134.24\,J\,mol^{-1}\,K^{-1}$ while an extrapolation of our experimental data yields $126.1\,J\,mol^{-1}\,K^{-1}$. This agreement is reasonable, but as thermodynamic modeling gives a much larger value ($149.55\,J\,mol^{-1}\,K^{-1}$, Xirouchakis et al. [20]) a further investigation seems to be warranted.

5. Acknowledgments

References

[1] J. A. Kuszyk, R. C. Brast, Influence of grain size on effects of thermal expansion anisotropy in $MgTi_2O_5$, Journal of the American Ceramic Society 56 (8) (1973) 420–423.

[2] H. J. Siebeneck, D. P. H. Hasselman, J. J. Cleveland, R. C. Bradt, Effects of grain size and microcracking on the thermal diffusivity of $MgTi_2O_5$, Journal of the American Ceramic Society 60 (1977) 336–338.

[3] M. Llusar, E. Garcia, M. T. Garcia, C. Gargori, J. A. Badenes, G. Monros, Synthesis, stability and coloring properties of yellow-orange pigments based on Ni-doped karrooite, Journal of the European Ceramic Society 35 (1) (2015) 357–376.

[4] J. F. W. Bowles, Definition and range of composition of naturally occurring minerals with the pseudo-brookite structure, American Mineralogist 73 (1988) 1377–1383.

[5] J. L. Hayob, E. J. Essene, Armalcolite in crustal paragneiss xenoliths, central Mexico, American Mineralogist 80 (1995) 810–822.

[6] S. Klemme, D. Günther, K. Hametner, S. Prowatke, T. Zack, The partitioning of trace elements between ilmenite, ulvospinel, armalcolite and silicate melts with implications for the early differentiation of the moon, Chemical Geology 234 (2006) 251–263.

[7] M. A. Reddy, M. S. Kishore, V. Pralong, V. Caignaert, U. V. Varadaraju, B. Raveau, Synthesis and lithium insertion into nanophase $MgTi_2O_5$ with pseudo-brookite structure, Chemistry of Materials 20 (6) (2008) 2192–2197.

[8] Y. Qu, W. Zhou, Y. Xie, L. Jiang, J.-Q. Wang, G.-H. Tian, Z.-Y. Ren, C.-G. Tian, H.-G. Fu, A novel phase-mixed $MgTiO_3$–$MgTi_2O_5$ heterogeneous nanorod for high efficiency photocatalytic hydrogen production, Chemical Communications 49 (2013) 8510–8512.

[9] F. Matteucci, G. Cruciani, M. Dondi, G. Gasparotto, D. M. Tobaldi, Crystal structure, optical properties and colouring performance of karrooite $MgTi_2O_5$ ceramic pigments, Journal of Solid State Chemistry 180 (11) (2007) 3196–3210.

[10] Y. Suzuki, T. S. Suzuki, Y. Shinoda, K. Yoshida, Uniformly porous $MgTi_2O_5$ with narrow pore-size distribution: XAFS study, improved in situ synthesis, and new in situ surface coating, Advanced Engineering Materials 14 (12) (2012) 1134–1138.

[11] P. N. Kapoor, S. Uma, S. Rodriguez, K. J. Klabunde, Aerogel processing of MTi$_2$O$_5$ (M = Mg, Mn, Fe, Co, Zn, Sn) compositions using single source precursors: synthesis, characterization and photocatalytic behavior, Journal of Molecular Catalysis A: Chemical 229 (1–2) (2005) 145–150.

[12] M. V. Reddy, G. V. Subba Rao, B. V. R. Chowdari, Metal oxides and oxysalts as anode materials for Li ion batteries, Chemical Reviews 113 (7) (2013) 5364–5457.

[13] F.-X. Xie, Y.-F. Deng, Y. Xie, H.-J. Xu, G.-H. Chen, Ultra-small nanoparticles of MgTi$_2$O$_5$ embedded in carbon rods with superior rate performance for sodium ion batteries, Chemical Communications 51 (2015) 3545–3548.

[14] I. Shindo, Determination of the phase diagram by the slow cooling float zone method: The system MgO–TiO$_2$, Journal of Crystal Growth 50 (4) (1980) 839–851.

[15] B. A. Wechsler, A. Navrotsky, Thermodynamics and structural chemistry of compounds in the system MgO–TiO$_2$, Journal of Solid State Chemistry 55 (2) (1984) 165–180.

[16] G. Eriksson, A. D. Pelton, Critical evaluation and optimization of the thermodynamic properties and phase diagrams of the CaO–Al$_2$O$_3$, Al$_2$O$_3$–SiO$_2$, and CaO-Al$_2$O$_3$–SiO$_2$ systems, Metallurgical Transactions B 24 (5) (1993) 807–816.

[17] Y. Suzuki, Y. Shinoda, Magnesium dititanate (MgTi$_2$O$_5$) with pseudobrookite structure: a review, Science and Technology of Advanced Materials 12 (3) (2011) 034301.

[18] N. E. Brown, A. Navrotsky, Structural, thermodynamic, and kinetic aspects of disordering in the pseudobrookite-type compound karrooite, MgTi$_2$O$_5$, American Mineralogist 74 (1989) 902–912.

[19] M. S. Ghiorso, H.-X. Yang, R. M. Hazen, Thermodynamics of cation ordering in karrooite MgTi$_2$O$_5$, American Mineralogist 84 (1999) 1370–1374.

[20] D. Xirouchakis, A. Smirnov, K. Woody, D. H. Lindsley, D. J. Andersen, Thermodynamics and stability of pseudobrookite-type MgTi$_2$O$_5$ (karrooite), American Mineralogist 87 (5–6) (2002) 658–667.

[21] A. R. Lennie, K. S. Knight, C. M. B. Henderson, Cation ordering in MgTi$_2$O$_5$ (karrooite): probing temperature dependent effects with neutrons, American Mineralogist 92 (2007) 1165–1180.

[22] H.-X. Yang, R. M. Hazen, Crystal chemistry of cation order-disorder in pseudobrookite-type MgTi$_2$O$_5$, Journal of Solid State Chemistry 138 (2) (1998) 238–244.

[23] M. D. Lind, R. M. Housley, Crystallization studies of lunar igneous rocks: crystal structure of synthetic armalcolite, Science 175 (1972) 521–523.

[24] A. Navrotsky, Thermodynamics of formation of some compounds with the pseudobrookite structure and of the $FeTi_2O_5$–Ti_3O_5 solid solution series, American Mineralogist 60 (1975) 249–256.

[25] G. Bayer, Thermal expansion characteristics and stability of pseudobrookite-type compounds, Me_3O_5, Journal of the Less Common Metals 24 (2) (1971) 129–138.

[26] H. Müller-Buschbaum, M. Waburg, Pseudobrookite mit weitgehend geordneter Metallverteilung: $CoTi_2O_5$, $MgTi_2O_5$ und $FeTi_2O_5$, Monatshefte für Chemie / Chemical Monthly 114 (1) (1983) 21–25.

[27] I. E. Grey, C. Li, I. C. Madsen, Phase equilibria and structural studies on the solid solution $MgTi_2O_5$–Ti_3O_5, Journal of Solid State Chemistry 113 (1) (1994) 62–73.

[28] R. D. Shannon, Revised effective ionic radii and systematic studies of interatomic distances in halides and chalcogenides, Acta Crystallographica A32 (1976) 751–767.

[29] R. M. Hazen, A. Navrotsky, Effects of pressure on order-disorder reactions, American Mineralogist 81 (1996) 1021–1035.

[30] R. M. Hazen, H.-X. Yang, Increased compressibility of pseudobrookite-type $MgTi_2O_5$ caused by cation disorder, Science 277 (5334) (1997) 1965–1967.

[31] B. A. Wechsler, R. B. Von Dreele, Structure refinements of Mg_2TiO_4, $MgTiO_3$ and $MgTi_2O_5$ by time-of-flight neutron powder diffraction, Acta Crystallographica Section B 45 (6) (1989) 542–549.

[32] Y. Suzuki, M. Morimoto, Uniformly porous $MgTi_2O_5$ with narrow pore-size distribution: in situ processing, microstructure and thermal expansion behavior, Journal of the Ceramic Society of Japan 118 (1384) (2010) 1212–1216.

[33] Y. Nakagoshi, Y. Suzuki, Morphology control of pseudobrookite-type $MgTi_2O_5$ powders by LiF doping, International Letters of Chemistry, Physics and Astronomy 46 (2015) 37–41.

[34] D. L. Zhang, Processing of advanced materials using high-energy mechanical milling, Progress in Materials Science 49 (3–4) (2004) 537–560.

[35] M. Sopicka-Lizer, High-energy ball milling: Mechanochemical processing of nanopowders, Woodhead publishing limited, 2010.

[36] H. P. Liermann, R. T. Downs, H.-X. Yang, Site disorder revealed through Raman spectra from oriented single crystals: A case study on karrooite ($MgTi_2O_5$), American Mineralogist 91 (5–6) (2006) 790–793.

[37] A. H. Karande, S. Y. Shingare, S. S. Gurav, S. V. Salvi, Influence of anatase and rutile phases on physical properties of new nanosize $MgTi_2O_5$, International Journal of Chemical and Physical Sciences 3 (2014) 17–20.

[38] A. H. Karande, S. Y. Shingare, S. S. Gurav, S. V. Salvi, Role of divalent substitution in dielectric behavior and pressure sensitivity of $MgTi_2O_5$, International Journal of Chemical and Physical Sciences 3 (2014) 1–9.

[39] S. S. Todd, Low temperature heat capacities and entropies at 298.16 K of magnesium orthotitanate and magnesium dititanate, Journal of the American Chemical Society 74 (1952) 4669–4670.

[40] A. Larson, R. B. Von Dreele, GSAS, 2004.

[41] B. H. Toby, EXPGUI, a graphical user interface for GSAS, Journal of Applied Crystallography 34 (2001) 210–213.

[42] C. M. B. Henderson, K. S. Knight, A. R. Lennie, Temperature dependence of rutile (TiO_2) and geikielite ($MgTiO_3$) structures determined using neutron powder diffraction, The Open Mineralogy Journal 3 (2007) 1–11.

[43] S. J. Clark, M. D. Segall, C. J. Pickard, P. J. Hasnip, M. J. Probert, K. Refson, M. C. Payne, First principles methods using CASTEP, Zeitschrift für Kristallographie 220 (2005) 567–570.

[44] J. P. Perdew, K. Burke, M. Ernzerhof, Generalized gradient approximation made simple, Physical Review Letters 77 (1996) 3865–3868.

[45] K. Refson, S. J. Clark, P. R. Tulip, Variational density functional perturbation theory for dielectrics and lattice dynamics, Physical Review B 73 (2006) 155114.

[46] D. V. Porezag, M. R. Pederson, Infrared intensities and Raman-scattering activities within density-functional theory, Phys. Rev. B 54 (1996) 7830–7836.

[47] V. Milman, M. C. Warren, Elasticity of hexagonal BeO, Journal of Physics: Condensed Matter 13 (2001) 241.

[48] P. Scherrer, Bestimmung der Größe und der inneren Struktur von Kolloidteilchen mittels Röntgenstrahlen, Nachrichten von der Gesellschaft der Wissenschaften zu Göttingen, Mathematisch-Physikalische Klasse 1918 (1918) 98–100.

[49] A. Patterson, The Scherrer formula for X-ray particle size determination, Physical Review 56 (1939) 978–982.

[50] E. Prince, Mathematical aspects of Rietveld refinement, in: R. A. Young (Ed.), The Rietveld Method, Oxford University Press, New York, 43–54, 1993.

[51] R. Hill, Data collection strategies: fitting the experiment to the need, in: R. A. Young (Ed.), The Rietveld Method, Oxford University Press, New York, 61–101, 1993.

[52] W. Kaminsky, WinTensor, Department of Chemistry, University of Washington, WA, URL `http://cad4.cpac.washington.edu/WinTensorhome/WinTensor.htm`, 2004.

[53] A. Navrotsky, O. J. Kleppa, The thermodynamics of cation distributions in simple spinels, Journal of Inorganic and Nuclear Chemistry 29 (11) (1967) 2701–2714.